

Accepted Manuscript

Influence of graphitic/amorphous coated carbon on HER activity of low temperature synthesized β -Mo₂C@C nanocomposites

Rameez Ahmad Mir, Om Prakash Pandey

PII: S1385-8947(18)30832-5
DOI: <https://doi.org/10.1016/j.cej.2018.05.041>
Reference: CEJ 19057

To appear in: *Chemical Engineering Journal*

Received Date: 23 January 2018
Revised Date: 15 April 2018
Accepted Date: 7 May 2018



Please cite this article as: R.A. Mir, O.P. Pandey, Influence of graphitic/amorphous coated carbon on HER activity of low temperature synthesized β -Mo₂C@C nanocomposites, *Chemical Engineering Journal* (2018), doi: <https://doi.org/10.1016/j.cej.2018.05.041>

This is a PDF file of an unedited manuscript that has been accepted for publication. As a service to our customers we are providing this early version of the manuscript. The manuscript will undergo copyediting, typesetting, and review of the resulting proof before it is published in its final form. Please note that during the production process errors may be discovered which could affect the content, and all legal disclaimers that apply to the journal pertain.

Influence of graphitic/amorphous coated carbon on HER activity of low temperature synthesized β -Mo₂C@C nanocomposites

Rameez Ahmad Mir^a and Om Prakash Pandey^{a*}

Affiliation^a: Functional materials lab, School of Physics and Materials Science, Thapar Institute of Engineering and Technology, Patiala-Punjab.

Corresponding author*: Dr. Om Prakash Pandey

Email: oppandey@thapar.edu

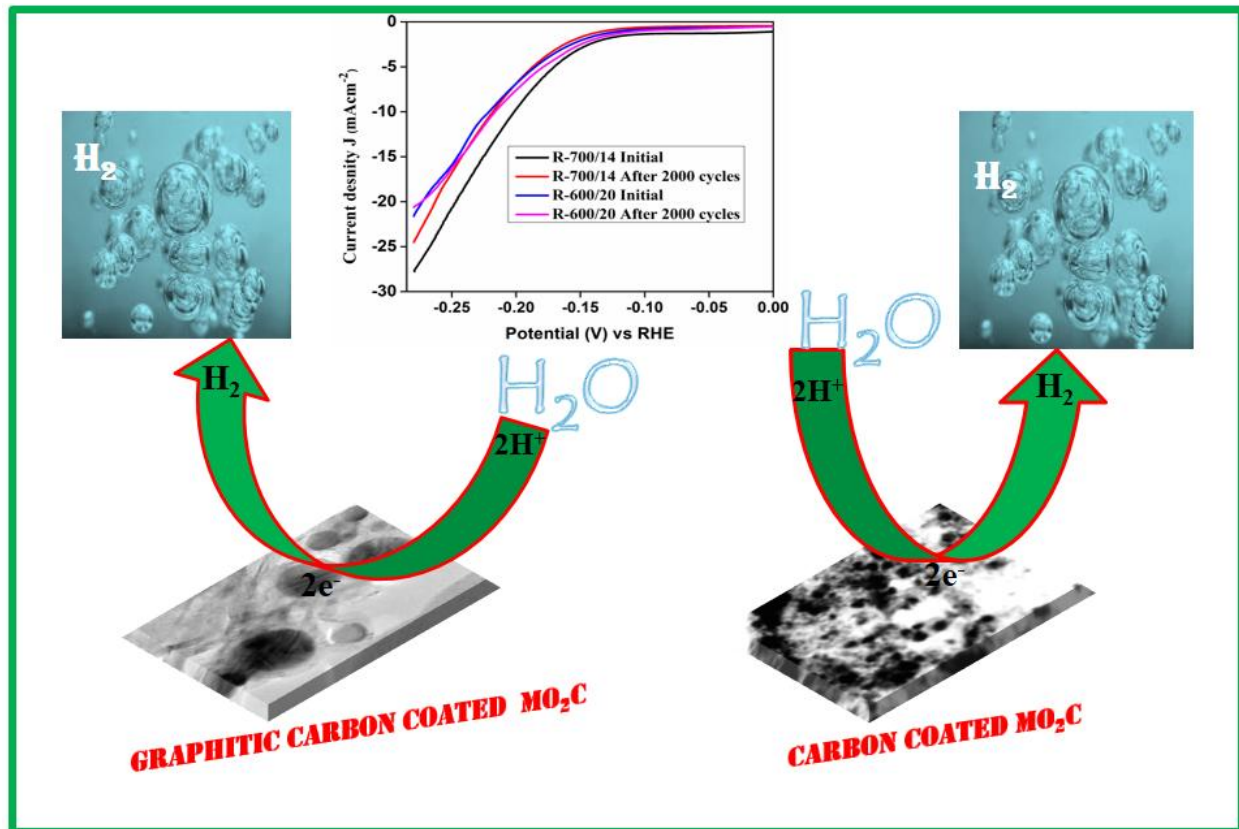
Tel: 0175-2393038

Abstract

The most economical and sustainable method for commercial scale production of hydrogen is through electrochemical water splitting. Though noble metal free catalysts for hydrogen evolution reaction (HER) are being developed to make water splitting more efficient, the search of highly efficient cost effective catalyst for HER still remains a challenge. Carbon coated molybdenum carbide composites (β -Mo₂C@C), a noble metal free electrocatalyst is being highly studied substance as potential electrocatalyst for water splitting where presence of graphitic carbon plays important role. Our study indicate that nature of carbon coating on Mo₂C surface plays vital role (amorphous/graphitic). In our systematic experiments β -Mo₂C@C was synthesized in an autoclave. The synthesis parameters were varied to get amorphous as well as graphitic coating on Mo₂C. The amorphous surface carbon shows better stability of electrocatalyst in acidic medium compared to graphitic coating. The electrochemical double-layer capacitance (EDLC) measurements suggest β -Mo₂C@C as suitable candidate for energy storage applications.

Keywords: Molybdenum carbide, carbon coating, nano-composite, waste plastics, carburization,

electrocatalyst, hydrogen evolution reaction.



Graphical representation of HER activity in presence of $\beta\text{-Mo}_2\text{C}@C$.

1. Introduction

To address the environmental issues caused due to the emission of harmful gases by traditional fossil fuels, different alternate sources of energy are being searched. The combustion of fossil fuels produces enormous toxic and harmful carbonaceous gases. The excess use of these fossil fuels is intensifying the air pollution, which affects human health and a cause of global warming. The solemnity of environmental issues and the increasing demand for energy with the limited supply of resources of fossil fuels have led to the development of new materials for energy production from natural or renewable sources.

The production of hydrogen by electrochemical water splitting can provide a clean and renewable energy resource [1] [2] [3] [4] [5]. For technologies with energy systems utilizing hydrogen and enabling zero emission of greenhouse gases, the cost and efficient water splitting is a critical issue [2] [5] [6]. The high-performance electrocatalysts are required in order to increase the efficiency of water splitting to promote the hydrogen evolution reaction (HER). Platinum (Pt) is the most efficient HER electrocatalyst, but the low abundance and high cost of Pt hinder its commercial use [7]. Various efforts have been made in last few decades for the development of low cost electrocatalysts for HER [5] [8] [9] [10] [11] [12].

Among the noble-metal free catalysts, molybdenum carbide ($\beta\text{-Mo}_2\text{C}$) is the fascinating candidate for electrocatalysis because of its low cost, high chemical stability and structural similarity to Pt group metals [13] [14] [15]. The insertion of carbon atom in the molybdenum metal lattice broadens the d-band structure, which resembles with Pt [16] [17]. $\beta\text{-Mo}_2\text{C}$ is stable and efficient electrocatalyst for HER in both acidic and basic mediums [18] [19]. The HER activity of $\beta\text{-Mo}_2\text{C}$ is greatly influenced by the surface structure and elemental composition,

which depends on the method of synthesis [20]. Mo₂C nanostructures have been synthesized via different methods to enhance their catalytic activities [12] [14] [21] [22].

Carbon support on Mo₂C in different forms improves the performance and stability of the composites [23] [24] [25] [26]. The nature of carbon encapsulating the β -Mo₂C particles plays an important role in the electrocatalytic activity of HER. The incorporation of these nanoscopic materials (β -Mo₂C) in the carbon frame is highly desirable. The structure, crystallite size, and morphology of carbide particles are dependent on the synthesis temperature, time, type, concentration and nature of carbon source [27]. The uniform carburization of carbide nanoparticles and inescapable agglomeration at high temperatures still remains an unsolved issue.

The present work reports the synthesis of carbon coated molybdenum carbide nano composite (β -Mo₂C@C) in an autoclave at low temperature. Polypropylene, a low cost thermoplastic polymer utilized for the manufacturing of various plastic products, which ends as waste material is used as carbon source. The utilization of these plastic waste or polypropylene will make the synthesized product cost effective and address the problems caused due to the disposal of these plastic wastes. Recycling is the current path followed to overcome the environmental issues caused due to the disposal of the plastic wastes. However, the recycling of plastic wastes emits poisonous gases, which affects the environment inherently. The emission of carbonaceous gases inside the autoclave serve as reaction gases and help in fast reduction-carburization of MoO₃ to form Mo₂C. This makes the process cost effective and environmentally friendly. A new process for the utilization of such waste to synthesize molybdenum carbide has been demonstrated and reported [28]. In order to bring down the cost of the product carbide phase further, experiments were performed at still lower temperatures. This further facilitates to have the smaller particle

size for a better electrocatalytic activity. The HER activity of the as synthesized sample β - $\text{Mo}_2\text{C}@\text{C}$ was investigated in acidic medium. The synthesized β - $\text{Mo}_2\text{C}@\text{C}$ shows higher stability and improved electrocatalytic HER performance in the acidic medium than the bulk and supported non-precious metal materials[29] [30]. It has been observed that the graphitic surface carbon improves the charge transfer kinetics whereas amorphous carbon enhances the stability of the electrocatalyst.

2. Materials and Methods

2.1 Experimental details

The carbon coated molybdenum carbide (β - $\text{Mo}_2\text{C}@\text{C}$) nanopowders have been synthesized with modified process parameters reported previously [28]. Here in the present work, 1.4394g of molybdenum trioxide (MoO_3), 3.5g magnesium (Mg) as reducing agent and 1g of polypropylene were mixed and sealed in a specially designed autoclave [31]. The properly sealed autoclave was put in a furnace and the temperature of the furnace was raised from room temperature to desired temperature 600 and 700 °C at the constant heating rate of 5 °C per minute. The temperature was maintained at 600 °C for 15, 17 and 20 hours to obtain single phase Mo_2C . In the second set of experiments, the temperature was maintained at 700 °C for 12 and 14 hours. The autoclave was then allowed to cool to room temperature and the obtained product was collected and washed with (1:1) diluted HCl to remove MgO. The resultant powder was washed with distilled water many times to remove the HCl followed by vacuum heating at 120 °C. Table1 gives the details of the reaction parameters with sample label and obtained major/minor phases.

2.2 Characterization

Samples so obtained were characterized by XRD using PANalytical X-Pert-Pro with $\text{CuK}\alpha$ radiation ($\lambda = 1.5406 \text{ \AA}$) using a copper target with an in-built Ni filter. The X-ray powder

diffraction data of all the samples were collected at room temperature between $20^{\circ} \leq 2\theta \leq 80^{\circ}$ with a step size of 0.0130° (2θ). The phase identification of the synthesized samples was done with the help of X-Pert High Score Plus using the ICDD data base. To estimate the degree of graphitization, the samples were analyzed by Raman spectroscopy STR 500 Airix. The microstructural and morphological studies of synthesized $\beta\text{-Mo}_2\text{C@C}$ powders were done under field- emission scanning electron microscope (FE-SEM) (*Hitachi SU 8010*) and transmission electron microscope (TEM) (*JEOL 2100 F*) operating at 15 kV and 200 kV, respectively. The elemental presence in the synthesized samples were characterized by energy dispersive spectra (EDS) of FESEM and scanning transmission electron microscopy (STEM) dot mapping through TEM. To study the surface chemical compositions and their valence states, the $\beta\text{-Mo}_2\text{C@C}$ samples were further analyzed by X-ray photoelectron spectroscopy (XPS). The measurements were carried out in XPS spectrometer (ESCA+) using Al-K α radiation (1486.7 eV), operating at 15 kV and 15mA. The C1s peak 284.6 eV was selected as the reference to calibrate the position of other peaks. The nitrogen adsorption/desorption studies were done with the help BEL-miniII operated at 77K to estimate Brunauer-Emmet-Teller (BET) surface area, the pore size and the pore volume using.

2.3 Electrochemical studies

The electrocatalytic activities of the as prepared samples towards HER were analyzed using three electrode cell. The working electrode was first fabricated using the following procedure:

1 mg of carbon coated molybdenum carbide composite ($\beta\text{-Mo}_2\text{C@C}$) was mixed with 250 μL of ethanol and sonicated for 25 minutes for uniform dispersion. 10 μL of the prepared solution was dropped on the top surface of the glassy carbon electrode (GCE) having a surface area of 0.070

cm². Finally, one drop of 10 μ L Nafion 117 solution (Sigma Aldrich) was dropped on the top surface and left over night for drying.

The electrocatalytic analysis was conducted using three electrode cell in Bio-logic EC Lab SP300 standard setup. The measurements were done using reversible hydrogen electrode (RHE) and high purity graphite rod as the reference and counter electrodes, respectively. All the electrodes were immersed in an electrolyte solution 0.5M H₂SO₄. Linear sweep voltammetry (LSV) were measured in between -0.28 and 0.185 V at the scan rate of 2mVs⁻¹. The cyclic voltammetry (CV) curves were measured at a scan rate 100 mVs⁻¹ for 2000 cycles in voltage range -0.28 to 0.2 V. To activate the surface of the catalyst and also to remove contamination and stabilize the electrochemical currents, the electrodes were pre-treated before HER analysis by CV between -0.3 to 0.3 V at a scan rate 50 mVs⁻¹ [32].

3 Results and Discussion

3.1 X-ray diffraction (XRD)

The typical X-ray diffraction pattern of sample synthesized at 600 °C for 15 hours (R-600/15) reveals the formation of intermediate mono molybdenum carbide (MoC) phase (ICDD pattern - 089-4305) as shown in Fig. 1a. The result shows that the carburization of MoO₃ occurred with the increase in reaction time beyond 10 hours [28]. Increasing the reaction time to 17 hours at 600 °C (R-600/17) does not make any change in product phase formation as shown in Fig. 1a. Only MoC phase of higher intensity was observed. When the reaction time was further increased to 20 hours at 600 °C (R-600/20), the formation of the pure phase Mo₂C (ICDD reference pattern - 035-0787) with impurity peaks corresponding to hexagonal carbon (ICDD reference pattern - 026-1076) as shown in Fig. 1a was observed. The reaction time of 12 hours at 700 °C (R-700/12) reveals the formation of Mo₂C along with impurity peak of Mo as shown in Fig. 1a. The results

indicate that the reduction has completed at 700 °C for 12 hours, but reaction time is not sufficient enough to accomplish the complete carburization of reduced Mo to Mo₂C. Increasing the reaction time to 14 hours at 700 °C (R-700/14) has led to the formation of pure crystalline phase Mo₂C as shown in Fig. 1a. The peaks at 34.4, 37.9, 39.4, 52.2, 61.6, 74.7 and 75.6 correspond to (100), (002), (101), (102), (110), (103), (112) and (201) planes of hexagonal molybdenum carbide (β -Mo₂C) phase. These results indicate that pure β -Mo₂C can be obtained at relatively lower temperature via the in-situ reduction-carburization route in the autoclave. The additional peaks at 26.6 in R-700/14 having low intensity and the peaks at 26.6 and 42.8 in R-600/20 are attributed to hexagonal carbon. The reaction temperature and time enhances the reduction and carburization to form pure carbide phase [33] [34] [35] [36]. The higher intensity peaks corresponding to Mo₂C in R-700/14 may be ascribed to more crystalline nature compared to R-600/20 [26]. The more crystalline nature of R-700/14 has been confirmed by lower full-width half maxima (FWHM) value as compared to R-600/20, shown in Fig. S1a and S2a (Supplementary information, SI), respectively. The higher amount of carbon present in R-600/20 determined by the prominent peak at ~26.6 may correspond to unreacted carbon present on the surface at the lower reaction temperature. The increase in reaction time at lower temperature enhances the carburization of reduced oxide phase because the carbon atoms present on the surface needs to travel a longer distance to form pure phase Mo₂C [36]. The decreased peak intensity of carbon in the as synthesized sample (R-700/14) may be attributed to the higher diffusion rate of carbon at higher reaction temperatures compared to R-600/20.

The XRD results of samples R-600/20 and R-700/14 confirm the pure phase formation of Mo₂C (Fig.1a). The data was fitted via Rietveld refinement for hexagonal space group P63/mmc (194) to confirm the crystal structure. Figure 1b shows the Rietveld refinement plots of the product

phase. The Wyckoff positions used for Rietveld refinement of XRD data are 2(c) $1/3, 2/3, 1/4$; $2/3, 1/3, 3/4$ for Mo and 2(a) $0,0,0$; $0,0,1/2$ for C [37]. The χ^2 values obtained from the Rietveld refinement for R-600/20 and R-700/14 are 2.1 and 1.93, respectively. The values of lattice parameters a, b and c as calculated from Rietveld refinement are $a = b = 3.013$, $c = 4.745$ for R-600/20, whereas for R-700/14 is $a = b = 3.016$, $c = 4.750$ for R-700/14/12/12, respectively,

3.2 Crystallite size and strain

X-ray line profile fitting technique using the Gaussian function estimated the peak position, 2θ (Bragg Peaks) and full-width half maxima β_{observed} of the diffraction peaks. The curve fit results for peak (100) of R-700/14 and (102) of R-600/20 are shown in Fig. S1a and S2b (SI), respectively. The breadth of peak incorporates both instrumental and sample dependent effects. Corresponding to diffraction peak of Mo_2C , the instrumental corrected broadening (β) was calculated from the following relation [38] :

$$\beta^2 = [(\beta^2)_{\text{observed}} - (\beta^2)_{\text{instrumental}}] \quad (1)$$

The crystallite size is estimated from the commonly used method Scherrer criterion, a volume weighted quantity. The Scherrer criterion utilizes full-width half maxima for determination of crystallite size (S) as given in equation S1, (SI) [39]. The calculated crystallite size (S) for as synthesized samples is given in Table 1. The Scherrer plot of R-700/14 and R-600/20 is shown in Fig. S1b and S2c, (SI) and the crystallite size (S) is calculated from the slope of the fit. The peak broadening in the said case is attributed to fine crystallite size.

3.3 William son Hall analysis

The peak broadening is merely due to strain was determined by a mathematical relation given by Stokes and Wilson [40]. The details of Williamson-Hall analysis has been demonstrated in appendix A , (SI) has been done utilizing uniform deformation model (UDM), uniform stress

deformation model (USDM) and uniform deformation energy density model (USEDM). UDM (equation S3, SI) considers strain to be isotropic in the whole crystal. The plot of ' $\beta \cos\theta$ ' as the function of ' $4 \sin\theta$ ' was fitted and the slope and intercept of fit measures the magnitude of micro strain ϵ and crystallite size, respectively as shown in Fig. S1c and S2d, (SI). The positive value of strain leads to compression within the lattice. However, the assumption of strain isotropy and homogeneity is not fulfilled in many cases, so USDM (equation S4, SI) and USED M (equation S6, SI), respectively were considered. All the three models in R-700/14 UDM (Fig.S1c, SI), USDM (Fig. S1d, SI) and USED M (Fig. S1e, SI) seems to be appropriate with less scattering of data from linear expression and the estimated values are given in Table 2. However, the UDM model (Fig. S1c, SI) is more precise with less scattering of data than USDM (Fig. S1d, SI) and USED M (Fig. S1e, SI), respectively. In R-600/20, the UDM model (Fig. S2d, SI) is more appropriate having less scattering of data than USDM (Fig. S2e, SI) and USED M (Fig. S2f, SI), respectively. The values so obtained are listed in Table 2. The extra carbon present in the system, with a prominent peak ~ 26.6 in R-600/20 may result in less strain value as compared to R-700/14 [36]. The presence of carbon hinders the further diffusion of carbon to attain a stable state of the system with low strain value. The increase in crystallite size from R-600/20 to R-700/14 is in accordance with the more crystalline nature of R-700/14.

3.4 Raman Spectroscopy

The degree of graphitization of $\beta\text{-Mo}_2\text{C}@C$ is determined by Raman spectra as shown in Fig. 2. The peak positions in Raman spectra located at ~ 1345 , 1580 and 2690 cm^{-1} correspond to induced disordered D-band, G-band and the 2D band of crystalline graphite, respectively [41]. The results predict the existence of the ordered graphitic carbon in the $\beta\text{-Mo}_2\text{C}@C$. The decrease in the ratio of ID/IG 0.88 to 0.23 for R-600/20 and R-700/14 suggest the increase in

graphitization of carbon with the increase in temperature [42]. Moreover, the increase in the intensity of 2D band in R-700/14 reveals that the crystalline graphitic carbon becomes more prominent at higher temperatures. The results indicate that R-600/20 contains more distorted or amorphous carbon in comparison to R-700/14. However, R-700/14 contains more graphitic carbon content.

3.5 Morphological studies

Figure 3 shows the FESEM micrographs of R-700/14 (a, b) and R-600/20 (c, d), respectively. The FESEM micrographs in Fig. 3 (a&c) elucidate that particles are highly agglomerated and have nearly spherical to faceted morphology. The results reveal that R-700/14 consists of bigger particle size as compared to R-600/20. However, the size uniformity seems to be more in R-600/20 as observed in the magnified image shown in Fig. 3d. The energy dispersive spectra (EDS) of FESEM confirms the presence of Mo and C (Fig. S3 a-b, SI) and the relative proportion of identified elements in weight percent is given in table S1 (SI). The particles in R-700/14 are connected through a carbon network shown in Fig 3(a, b). The carbon network observed in TEM (Fig. 4a) consists of the graphitic carbon as shown in HRTEM (Fig. 4b) for R-700/14. The inset in Fig.4b elucidates the lattice fringes of 0.22 nm corresponding to (101) plane of Mo_2C (ICDD reference pattern-035-0787). The coated and wrapped graphitic carbon encapsulating Mo_2C particles correspond to (002) plane having lattice fringes 0.32 nm in accordance with the d spacing of ICDD reference pattern -026-1076 and -001-0640. The HRTEM micrographs in Fig. 4b reveals the graphitic sheets and tubules like growth morphology of carbon as observed by Iijima *et al.* [43]. The EDS elemental mapping of STEM shown in Fig. 4 (c-f) predicts the spatial distribution of Mo and C elements with exception of small amount of oxygen. The individual distribution of elements is shown in Fig. 4d (Mo), Fig. 4e (C) and Fig. 4f (O), respectively. However, in the case of R-600/20, the particles are encapsulated in thick carbon layers as shown in Fig 5a. The HRTEM micrograph of R-600/20 shown in Fig. 5b reveals the presence of more amorphous carbon content as compared to R-700/14. The lattice fringing 0.22 nm and 0.18 nm correspond to (101) and (102) plane of Mo_2C (-035-0787 ICDD pattern). However, it also shows the presence of amorphous carbon coating around Mo_2C particles. The

deposition of more amorphous carbon content in R-600/20 is in accordance with the low synthesis temperature as compared to R-700/14 [43]. The EDS elemental mapping of STEM shows the more spatial distribution of Mo and C except for a lesser amount of oxygen present within the carbon matrix. However, the oxygen content in R-600/20 is more as compared to R-700/14. The Mo and C are more uniformly distributed in R-600/20 than R-700/14 as shown in Fig. 5 (c-f). The individual elemental distribution of Mo, C and O are given in Fig. 5d, Fig. 5e and Fig. 5f, respectively. The variation of oxygen content from case to core in the observed spectra indicate that the reduction-carburization of MoO_3 to Mo_2C occurs via formation of intermediate oxide and Mo metal reported elsewhere [28]. Figure 6 (a-b) shows the wide particle size distribution as observed from TEM images. More than 100 particles from different areas/scans were measured and the particle size follows lognormal distribution as given in equation S7 (SI). The particle size calculated from TEM is comparable to that calculated from XRD (W-H) analysis. The results indicate that deviation in particle size using different models may be the consequence of agglomeration of particles [33]. Moreover, the TEM and HRTEM results reveal more graphitic carbon content in R-700/14 and higher amorphous carbon content in R-600/20, which has also been predicted in Raman analysis. The carbon content in both the forms is expected to affect the HER activity differently.

3.5 X-ray photoelectron spectroscopy (XPS) analysis

The identification of chemical composition and surface chemistry of carburized products R-700/14 and R-600/20 were determined by peak deconvolution of X-ray photoelectron spectroscopy (XPS) data. The full survey spectrum of the spectrum of R-700/14 and R-600/20 is shown in Fig.7 (a-b), respectively. The presence of five distinct peaks for both R-700/14 and R-600/20 at positions 231.8, 282.4, 399.5 and 528.6 eV correspond to $\text{Mo}3d$, $\text{C}1s$, $\text{Mo}3p$, and $\text{O}1s$,

respectively [44]. The distribution of Mo species and corresponding oxidation states were determined by means of curve fitting. The high resolution (HR) spectra of Mo3d (R-700/14) is shown in Fig. 7c. The peaks observed at positions 228.1 and 231.8 eV attributed to (Mo^{2+}) $\text{Mo3d}_{5/2}$ and $\text{Mo3d}_{3/2}$, respectively reveals the formation of Mo_2C . An additional peak at 232.4 eV assigned to (Mo^{4+}) $\text{Mo3d}_{3/2}$ originated from MoO_2 . In addition to this, the peaks observed at 232.2 and 235.5 eV are attributed to (Mo^{6+}) $\text{Mo3d}_{5/2}$ and $\text{Mo3d}_{3/2}$, respectively [45]. This is the consequence of surface oxidation of Mo_2C surface when exposed to air for the prolonged duration [46] [26]. However, the HR spectra of Mo3d (R-600/20) in Fig. 7d shows the presence of (Mo^{2+}) $\text{Mo3d}_{5/2}$ and $\text{Mo3d}_{3/2}$ stemming from Mo_2C at peak positions 228.1 and 231.8 eV, respectively. In parallel, the peaks observed at 232.1 and 235.4 eV corresponds to (Mo^{6+}) $\text{Mo3d}_{5/2}$ and $\text{Mo3d}_{3/2}$ of MoO_3 , respectively. An additional peak at position 232.6 eV attributed to (Mo^{4+}) $\text{Mo3d}_{3/2}$ originated from MoO_2 . The superficial oxidation in the air might have resulted in the formation of these oxide species. However, the existence of MoO_2 may correspond to the presence of inherent oxide species within the carbon matrix. The HR of C1s spectra for R-700/14 and R-600/20 is shown in Fig S4 (a&c, SI). The deconvoluted peaks of C1s of both (R-700/14 and R-600/20) at 284.2 and 285.1 are assigned to Mo-C and C-C, respectively. The HR spectra O1s for both the samples (R-700/14 and R-600/20) is shown in Fig. S4 (b&d, SI), respectively. The deconvoluted peaks at positions 530.2 eV in both the samples are attributed to Mo-O. The peak attained at 531.6 and 531.8 eV in R-700/14/12/12 and R-600/20, respectively correspond to C-O [45]. However, the peaks observed at 532.4 in (R-700/14) and 532.9 in (R-600/20) have originated from C=O [47]. The high intensity of C1s and O1s spectra in R-600/20 predicts the higher content of carbon and oxygen in comparison to R-700/14. The same was observed in EDS

elemental mapping also. The elemental composition of Mo, C and O estimated from XPS analysis is given in Table S2 (SI).

ACCEPTED MANUSCRIPT

3.6 Nitrogen adsorption/desorption analysis (BET)

The Brunauer-Emmet-Teller (BET) specific surface area of R-700/14 and R-600/20 samples were estimated with the help of N₂ adsorption/desorption measurements. The measured BET specific surface area of β -Mo₂C@C (R-700/14 sample) is 20.9 m²g⁻¹ along with the mean pore size 14.4 nm and pore volume 0.16 cm³g⁻¹, respectively. However, R-600/20 sample exhibits BET specific surface area 60.8 m²g⁻¹ along with the mean pore size of 15 nm similar to R-700/14 and total pore volume of 0.292 cm³g⁻¹, respectively. The surface area decreases with the increase in temperature, which is in agreement with the crystallite size trend calculated with Scherrer equation in XRD pattern (Table 1). The higher crystallite size as observed in R-700/14 sample with the increase in the reaction temperature apparently decreases the specific surface area [48] [49]. Figure S5 (a-b, SI) shows the adsorption/desorption isotherms and mean pore size distribution of R-700/14 and R-600/20 samples, respectively. The surface area of R-700/14 decreased as compared to R-600/20. This might be because of higher crystallite size and degree of graphitization of particle surface with the increase in temperature, as observed in Raman spectra [50]. The internal pore strain or pore rupture also results in the decrease in surface area as the temperature is increased [51]. Moreover, the decrease in total pore volume may also result from agglomeration and sintering of particles with the rise in temperature [49] [52]. The presence of low carbon content in R-700/14 as compared to R-600/20 observed in XRD and XPS may result in the decrease in surface area because of the porous nature of surface carbon. The adsorption isotherms in Fig S5a (SI) of both the samples demonstrate the characteristic of a type-II isotherm, as per IUPAC classification [53] [54]. The isotherms observed in the present study shows characteristic of H-4 hysteresis [54] [55]. This indicates that there is formation of the

complex structure with mesopores and micropores, for both the samples as shown in Fig. S5 b (SI). This phenomenon might be associated with the agglomeration of particles in the final product. The effect of surface area and carbon present on the surface on the electrochemical properties of β - $\text{Mo}_2\text{C}@\text{C}$ has been studied in detail and presented below.

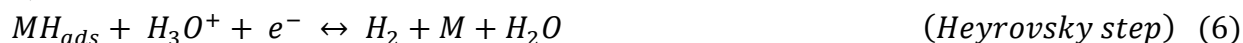
3.7 Electrocatalytic HER performance

The electrocatalytic HER activity of as synthesized samples were studied by linear sweep voltammetry (LSV). The LSV plots of intermediate product MoC (R-600/15 and R-600/17) shows the current density value 18.5 and 30.0 mAcm^{-2} , respectively given in Fig. S6 (a-b, SI). This reveals the increment in value of current density with increase in reaction time. The high current density values of R-600/15 and R-600/17 might be due to the lower crystallite size as calculated from XRD analysis. Moreover, the increase in reaction time favors the carburization process and crystallization of the product phase. The incorporation of C in the Mo lattice resembles its d-band structure with Pt and hence enhance the current density. It also favors the graphitization of surface carbon and hence enhances the charge transfer rate and increases the current density. The critical factor for HER catalysts is their long term stability. To probe the stability of the electrocatalyst R-600/15 and R-600/17, cyclic voltammetry (CV) measurements were performed in voltage range 0.2 to -0.28 V for 2000 cycles at the scan rate of 100 mVS^{-1} . The polarization curve obtained after 2000 cycles are shown in Fig. S6 (a-b, SI). The results depict the decrease in current density to 14.0 and 23.0 mAcm^{-2} for R-600/15 and R-600/17, respectively. The results predict that intermediate MoC phase are not stable HER electrocatalyst for long term durability. Whereas samples synthesized at same temperature for higher holding time (20 hours) leading to Mo_2C phase (R-600/20) encapsulated in carbon matrix exhibits the current density of 21 mAcm^{-2} as shown in Fig.8a. The polarization curve almost remains the

same in R-600/20 after 2000 cycles as shown in Fig. 8a. The pure phase Mo_2C (R-600/20) encapsulated in carbon coating, although having low current density value as compared to R-600/17 has higher stability with negligible loss of current after 2000 CV cycles. The lower current density of R-600/20 in comparison to R-600/17 might be consequence of bigger crystallite size (S). To probe the effect of temperature on electrocatalytic activity, the samples synthesized at 700 °C were analyzed. The sample having an impurity phase of Mo along with major phase Mo_2C (R-700/12), shows enhancement in current density value (23.5 mAcm^{-2}) with increase in reaction temperature as shown in Fig. S6c (SI). The current density value decreases by 24% after 2000 cycles as shown in Fig. S6c (SI). This reveals that Mo_2C along with impurity phase Mo (R-700/12) are not stable catalysts for HER. However, increasing the time at the same temperature leading to pure phase Mo_2C (R-700/14) further enhances the current density value to 27.9 mAcm^{-2} as shown in Fig. 8a. The long term stability of R-700/14 depicts the decrease in the current density after 2000 CV cycles by 10 % as shown in Fig. 8a. The pure phase Mo_2C coated with carbon (R-700/14) is less stable in comparison to R-600/20. The R-700/14 having the low surface area as compared to R-600/20 shows enhanced current density value. The increase in current density is in agreement with the increase in lattice strain from R-600/20 to R-700/14 (Table 2) [56] [57]. The strained nano $\text{Mo}_2\text{C}@C$ shows variation in d-band structures, which enhances the current density [57]. The more crystalline nature of R-700/14 and more graphitic carbon on the surface in comparison to R-600/20 enhances the electron transfer rate and hence improves the HER activity [23]. The coated graphitic carbon residue on the surface of Mo_2C acts as the supporting matrix and enhances the electrical conductivity or charge transfer capacity of the electrocatalyst [42] [58]. The low value of the current density of R-600/20 having the high surface area as compared to R-700/14 might be because of the more carbon on the surface as

determined by a prominent peak in XRD (graphitic and amorphous) and less graphitic carbon content as observed in Raman spectroscopy. The more amorphous carbon in R-600/20 has also been observed in TEM/HRTEM analysis and this deteriorates the catalytic performance of the electrocatalyst [42]. The porous carbon matrix support of β -Mo₂C@C particles prevents them from aggregation during reaction process and hence increases the stability [23]. However, R-600/20 having higher distorted carbon (amorphous) as compared to R-700/14 might render an extra protection [25]. The Mo₂C phase embedded in the amorphous carbon matrix might be not performing actively due to extra protection of carbon resulting in decrease in current density with higher stability [14]. The high durability of the catalyst originated from the coupling between the surface carbon and enclosed Mo₂C particles. The tight binding of carbon support and Mo₂C particles occurring during in-situ synthesis also improves the durability of the catalyst [59]. Moreover, the presence of more oxygen content in R-600/20 within the carbon matrix as observed in EDS STEM mapping results in enhancement of stability by creating a layer of oxide species, which inhibits further degradation of the active particle [60]. This also results in the decrease of current density because of low efficiency of these oxide phases towards HER.

The Tafel slope (b) is an inherent property of the catalyst surface and is extracted from Tafel plot as shown in Fig. S6d (SI) and Fig 8b. The value of b determines the probable mechanism of HER on the surface of the catalyst [11]. The value of HER in acidic medium follows the following steps [61] [62]:



Where ' M ' is the active site and MH_{ads} denote the hydrogen absorbed on that site. The value of Tafel slope (b) up to 120 mVdec^{-1} suggests that Volmer reaction (5) is rate determining step, otherwise, the value of b about 40 and 30 mVdec^{-1} is referred to Heyrovsky (6) and Tafel (7) reactions, respectively[23]. The value of b shown in Fig. S6d (SI) for MoC phase (R-600/15 and R-600/17) is 100.4 and 79.5 mVdec^{-1} , respectively. However, the value of b (Fig. S6d, SI) for impure phase R-700/12 is $115.13 \text{ mVdec}^{-1}$. The value of b (Fig. 8b) for R-700/14 and R-600/20 ($\beta\text{-Mo}_2\text{C@C}$) is 93.2 and 91.1 mVdec^{-1} , respectively and is consistent with the literature [29]. The decrease in value of b from MoC to pure (Mo_2C) phase formation reveals the faster reaction kinetics at the surface of product phase. The values b for both (R-700/14 and R-600/20) are almost similar, which signifies that discharge reaction is slow and rate of reaction is determined by Volmer step [23]. A little low value of b for R-600/20 may be a result of the higher surface area, which provides more active sites and enhances the rate of reaction. The as prepared samples show enhanced HER results, having the lower value of b as compared to previously reported results as given in Table S3 (SI). The decrement in the value of b (78.6 mVdec^{-1}) in R-700/14 after 2000 cycles signifies the higher electron transfer rate on the graphitic carbon surface and hence the rate of reaction tends towards Volmer-Heyrovsky step. However, in R-600/20 the value almost remains the same 90.0 mVdec^{-1} . This could be the result of excess carbon on the surface, which only promotes the stability and retains Volmer reaction as the rate determining step. This also signifies the low covering of hydrogen species on the surface and that hydrogen is weakly absorbed [61] [63]. The comparison of the overpotential, onset potential and the exchange current density calculated for the synthesized samples [5,11] are given in Table S3 (SI). Among the synthesized Mo_2C samples, R-700/14 exhibits lower overpotential and onset potential as compared to R-600/20. This might be the result of conducting graphitic surface

carbon which enhance the charge transfer rate at lower potentials. However, the lower onset and overpotential and higher exchange current density of MoC phase (R-600/17) corresponds to lower crystallite size.

The electrochemical surface area (ECSA)/ electrochemical double-layer capacitance (EDLC, C_{dl}) measurements were done via CV analysis performed in voltage range 0.2 to 0.4 V at different scan rates (20-230 mVs^{-1}) is shown in Fig. 9 (a-e). The plot of scan rate (mVs^{-1}) on the x-axis and current density $\Delta j_{0.3}$ ($mAcm^{-2}$) on the y-axis for R-600/15/, R-600/17, R-700/12 are shown in Fig. S7 (SI). However, for the pure phase $Mo_2C@C$ (R-600/20 and R-700/14) are presented in Fig. 9f.

The MoC has C_{dl} (Fig. S7, SI) values of 10.9 and 35.5 $mFcm^{-2}$ for R-600/15 and R-600/17, respectively. The higher ECSA of R-600/17 is responsible for higher current density and low value of Tafel slope as observed in LSV measurements and Tafel plots, respectively. The C_{dl} value for R-700/12 is about 11.0 $mFcm^{-2}$. The decrement in the value of ESCA with the rise in temperature might be because of surface sintering and thus inhibiting the active sites. The β - $Mo_2C@C$ has C_{dl} values of 12.5 and 30.0 $mFcm^{-2}$ for R-700/14 and R-600/20 (Fig. 9f), respectively. R-600/20 has about 2.5 times C_{dl} value as that of R-700/14, which is inconsistent with the high BET specific surface area of R-600/20. The higher C_{dl} values of R-600/17 and R-600/20 predict the synthesized material suitable for super capacitors. The BET surface area was not the sole reason affecting HER or ESCA. However, the morphological features, composition, and environment of active sites affect the same [64]. The lower value of the current density of R-600/20 although having the higher value of C_{dl} may also be a consequence of excess carbon and high oxygen content in the material.

The electrochemical impedance spectroscopy (EIS) of R-700/14 and R-600/20 were done to gain further insight about HER activity of synthesized Mo_2C nano powders encapsulated in carbon matrix. Figure S8 (a-b, SI) shows the Nyquist plot of R-700/14 and R-600/20 at different applied potentials (20-300 mV vs RHE). The near semi-circular curves observed at different potentials estimates the charge transfer resistance of both the samples. The semicircular curve of smaller diameter formed at higher potentials shows that charge transfer resistance (R_{ct}) decreases with increase in potential [26] [58]. This reflects the kinetics of HER process and depicts superior hydrogen evolution with applied potential. Deviation from the semicircular fit corresponding to an equivalent circuit to calculate value of resistance (R_{ct}) and other parameters may be attributed to surface inhomogeneity, roughness (variable capacitance across surface), electrode porosity (wide/uneven pore size) and surface reactivity [65,66]. In case of R-700/14, the graphitic carbon layer enclosing the particle acts as the electronic bridge and enhances the electron transfer on the surface and electronic conductivity of electrocatalyst [58]. The interconnection between Mo_2C and graphitic surface carbon decreases the contact electrical resistance, which leads to enhancement in electron transfer along each microstructure. The Bode plots of R-700/14 and R-600/20 are shown in Fig. S8 (c-d, SI). The phase angle and the total impedance becomes smaller at higher frequencies and shows similar impedance properties with regard to the HER potentials. However, the semicircular curve observed in both the cases shows potential dependency at higher values. The decrease and the shifting of phase angle towards higher frequencies indicates the lower resistance and superior HER kinetics.

Conclusion

Carbon coated molybdenum carbide nano composites ($\beta\text{-Mo}_2\text{C@C}$) were successfully synthesized in an autoclave at low temperature 600 and 700 °C for 12 and 20 hours, respectively.

The results predict the encapsulation of the Mo_2C particles within the carbon matrix. The graphitic carbon content and crystallite size increase with the temperature. Moreover, the strain increases with temperature as evidenced from Williamson-Hall analysis. The samples synthesized at low temperature have more size uniformity. The higher graphitic content enhances the charge transfer on the electrocatalyst surface, which enhances the HER activity. However, the sample synthesized at low temperature shows more stability in acidic medium. The presence of amorphous carbon and some oxide content within the carbon matrix enhances the stability of the electrocatalyst. The higher bonding between the Mo_2C and coated carbon produced during the in-situ synthesis enhances the HER efficiency and stability of the electrocatalyst. The ESCA estimated from EDLC measurements were in agreement with BET results. The EDLC results indicate the broad application of ($\beta\text{-Mo}_2\text{C@C}$) in energy storage systems. The specific surface area is not the sole reason for HER activity, but the structural and surface features influence the electrocatalytic performance. The charge transfer resistance decreases with increase in potential. The encapsulation of nanoparticle within the graphitic carbon matrix showed improved EIS results. The synthesis of other noble metal free catalyst by the aforementioned method will be cost effective and environmentally friendly. The work demonstrates that use of waste polypropylene (plastics) will provide significant economic and environment options in the conversion of waste plastic materials into highly useful and valuable materials.

Acknowledgement

The authors are grateful to SAI labs, Thapar University for providing XRD analysis. Authors express special thanks to Dr. Anup Thakur, Assistant professor Punjabi University, Patiala for providing the valuable suggestions and time in carrying out the Rietveld refinement. The authors are thankful to SAIF, Punjab University, Chandigarh for FESEM analysis. Authors express

special gratitude to Dr. Gajender Saini, AIRF, JNU, NewDelhi TEM and HRTEM analysis. Authors also thanks UGC-DAE Consortium (CSR-IC-239/2017-18/1320) for carrying this work under the scheme.

ACCEPTED MANUSCRIPT

References

- [1] C. Bae, T.A. Ho, H. Kim, S. Lee, S. Lim, M. Kim, H. Yoo, J.M. Montero-Moreno, J.H. Park, H. Shin, Bulk layered heterojunction as an efficient electrocatalyst for hydrogen evolution, *Sci. Adv.* 3 (2017) 1602215. doi:10.1126/sciadv.1602215.
- [2] J. a Turner, Sustainable hydrogen production., *Science*. 305 (2004) 972–974. doi:10.1126/science.1103197.
- [3] J. Kibsgaard, Z. Chen, B.N. Reinecke, T.F. Jaramillo, Engineering the surface structure of MoS₂ to preferentially expose active edge sites for electrocatalysis, *Nat. Mater.* 11 (2012) 963–969. doi:10.1038/nmat3439.
- [4] H.M. Chen, C.K. Chen, R.-S. Liu, L. Zhang, J. Zhang, D.P. Wilkinson, Nano-architecture and material designs for water splitting photoelectrodes, *Chem. Soc. Rev.* 41 (2012) 5654–5671. doi:10.1039/c2cs35019j.
- [5] X. Zou, Y. Zhang, Noble metal-free hydrogen evolution catalysts for water splitting, *Chem. Soc. Rev.* 44 (2015) 5148–5180. doi:10.1039/C4CS00448E.
- [6] I.P. Jain, Hydrogen the fuel for 21st century, *Int. J. Hydrogen Energy*. 34 (2009) 7368–7378. doi:10.1016/j.ijhydene.2009.05.093.
- [7] H.B. Gray, Powering the planet with solar fuel., *Nat. Chem.* 1 (2009) 7. doi:10.1038/nchem.141.
- [8] M.-R. Gao, Z.-Y. Lin, T.-T. Zhuang, J. Jiang, Y.-F. Xu, Y.-R. Zheng, S.-H. Yu, Mixed-solution synthesis of sea urchin-like NiSe nanofiber assemblies as economical Pt-free catalysts for electrochemical H₂ production, *J. Mater. Chem.* 22 (2012) 13662. doi:10.1039/c2jm31916k.
- [9] Z. Wu, B. Fang, A. Bonakdarpour, A. Sun, D.P. Wilkinson, D. Wang, WS₂ nanosheets as

- a highly efficient electrocatalyst for hydrogen evolution reaction, *Appl. Catal. B Environ.* 125 (2012) 59–66. doi:10.1016/j.apcatb.2012.05.013.
- [10] H. Fei, J. Dong, M.J. Arellano-Jiménez, G. Ye, N. Dong Kim, E.L.G. Samuel, Z. Peng, Z. Zhu, F. Qin, J. Bao, M.J. Yacaman, P.M. Ajayan, D. Chen, J.M. Tour, Atomic cobalt on nitrogen-doped graphene for hydrogen generation, *Nat. Commun.* 6 (2015) 8668. doi:10.1038/ncomms9668.
- [11] D.J. Li, U.N. Maiti, J. Lim, D.S. Choi, W.J. Lee, Y. Oh, G.Y. Lee, S.O. Kim, Molybdenum sulfide/N-doped CNT forest hybrid catalysts for high-performance hydrogen evolution reaction, *Nano Lett.* 14 (2014) 1228–1233. doi:10.1021/nl404108a.
- [12] L. Liao, S. Wang, J. Xiao, X. Bian, Y. Zhang, M.D. Scanlon, X. Hu, Y. Tang, B. Liu, H.H. Girault, A nanoporous molybdenum carbide nanowire as an electrocatalyst for hydrogen evolution reaction, *Energy Environ. Sci.* 7 (2014) 387–392. doi:10.1039/C3EE42441C.
- [13] S.T. Oyama, Preparation and catalytic properties of transition metal carbides and nitrides, *Catal. Today.* 15 (1992) 179–200. doi:10.1016/0920-5861(92)80175-M.
- [14] H.-B. Wu, B.-Y. Xia, L. Yu, X.-Y. Yu, W.-X.D. Lou, Porous molybdenum carbide nano - octahedrons synthesized via confined carburization in metal - organic frameworks for efficient hydrogen production, *Nat. Commun.* 6 (2015) 1–12. doi:10.1038/ncomms7512.
- [15] E.C. Weigert, D. V Esposito, J.G. Chen, Cyclic voltammetry and X-ray photoelectron spectroscopy studies of electrochemical stability of clean and Pt-modified tungsten and molybdenum carbide (WC and Mo₂C) electrocatalysts, 193 (2009) 501–506. doi:10.1016/j.jpowsour.2009.04.020.
- [16] R. B. Levy and M. Boudart, Platinum-Like Behavior of Tungsten Carbide in Surface

- Catalysis, Science (80-.). 181 (1973) 547–549.
- [17] G. Singla, K. Singh, O.P. Pandey, ScienceDirect Synthesis of carbon coated tungsten carbide nano powder using hexane as carbon source and its structural , thermal and electrocatalytic properties, *Int. J. Hydrogen Energy*. 40 (2015) 5628–5637.
doi:10.1016/j.ijhydene.2015.02.127.
- [18] H. Vrubel, X. Hu, Molybdenum boride and carbide catalyze hydrogen evolution in both acidic and basic solutions, *Angew. Chemie - Int. Ed.* 51 (2012) 12703–12706.
doi:10.1002/anie.201207111.
- [19] Y.C. Kimmel, X. Xu, W. Yu, X. Yang, J.G. Chen, Trends in electrochemical stability of transition metal carbides and their potential use as supports for low-cost electrocatalysts, *ACS Catal.* 4 (2014) 1558–1562. doi:10.1021/cs500182h.
- [20] T. Xiao, A.P.E. York, V.C. Williams, H. Al-megren, A. Hanif, X. Zhou, M.L.H. Green, Preparation of Molybdenum Carbides Using Butane and Their Catalytic Performance, (2000) 3896–3905. doi:10.1021/cm001157t.
- [21] W.-F. Chen, C.-H. Wang, K. Sasaki, N. Marinkovic, W. Xu, J.T. Muckerman, Y. Zhu, R.R. Adzic, Highly active and durable nanostructured molybdenum carbide electrocatalysts for hydrogen production, *Energy Environ. Sci.* 6 (2013) 943–951.
doi:10.1039/C2EE23891H.
- [22] C. Ge, P. Jiang, W. Cui, Z. Pu, Z. Xing, A.M. Asiri, A.Y. Obaid, X. Sun, J. Tian, Shape-controllable synthesis of Mo₂C nanostructures as hydrogen evolution reaction electrocatalysts with high activity, *Electrochim. Acta.* 134 (2014) 182–186.
doi:10.1016/j.electacta.2014.04.113.
- [23] Y.P. Mu, Y. Zhang, L. Fang, L. Liu, H.J. Zhang, Y. Wang, Controllable synthesis of

- molybdenum carbide nanoparticles embedded in porous graphitized carbon matrixes as efficient electrocatalyst for hydrogen evolution reaction, *Electrochim. Acta.* 215 (2016) 357–365. doi:10.1016/j.electacta.2016.08.104.
- [24] R. Ma, Y. Zhou, Y. Chen, P. Li, Q. Liu, J. Wang, Ultrafine molybdenum carbide nanoparticles composited with carbon as a highly active hydrogen-evolution electrocatalyst, *Angew. Chemie - Int. Ed.* 54 (2015) 14723–14727. doi:10.1002/anie.201506727.
- [25] K. Zhang, C. Li, Y. Zhao, X. Yu, Y. Chen, Porous one-dimensional Mo₂C-amorphous carbon composites: high-efficient and durable electrocatalysts for hydrogen generation., *Phys. Chem. Chem. Phys.* 17 (2015) 16609–14. doi:10.1039/c5cp02028j.
- [26] J.-S. Li, Y. Wang, C.-H. Liu, S.-L. Li, Y.-G. Wang, L.-Z. Dong, Z.-H. Dai, Y.-F. Li, Y.-Q. Lan, Coupled molybdenum carbide and reduced graphene oxide electrocatalysts for efficient hydrogen evolution., *Nat. Commun.* 7 (2016) 11204. doi:10.1038/ncomms11204.
- [27] T. Mo, J. Xu, Y. Yang, Y. Li, Effect of carburization protocols on molybdenum carbide synthesis and study on its performance in CO hydrogenation, *Catal. Today.* 261 (2016) 101–115. doi:10.1016/j.cattod.2015.07.014.
- [28] R.A. Mir, P. Sharma, O.P. Pandey, Thermal and structural studies of carbon coated Mo₂C synthesized via in-situ single step reduction-carburization, *Sci. Rep.* 7 (2017) 3518. doi:10.1038/s41598-017-03197-8.
- [29] K. Zhang, Y. Zhao, D. Fu, Y. Chen, Molybdenum carbide nanocrystal embedded N-doped carbon nanotubes as electrocatalysts for hydrogen generation, *J. Mater. Chem. A.* 3 (2015) 5783–5788. doi:10.1039/C4TA06706A.
- [30] Z. Yu, Y. Duan, M. Gao, C. Lang, Y. Zheng, S.-H. Yu, A one-dimensional porous carbon-

- supported Ni/Mo 2 C dual catalyst for efficient water splitting, *Chem. Sci.* 8 (2017) 968–973. doi:10.1039/C6SC03356C.
- [31] H. Singh, O.P. Pandey, Novel process for synthesis of nanocrystalline WC from wolframite ore, *Ceram. Int.* 41 (2015) 10481–10487. doi:10.1016/j.ceramint.2015.04.135.
- [32] C.Y. He, J.Z. Tao, Two-dimensional TaC nanosheets on a reduced graphene oxide hybrid as an efficient and stable electrocatalyst for water splitting, *Chem. Commun.* 52 (2016) 8810–8813. doi:10.1039/c6cc03876j.
- [33] A. Gupta, G. Singla, O.P. Pandey, Effect of synthesis parameters on structural and thermal properties of NbC / C nano composite synthesized via in-situ carburization reduction route at low temperature, *Ceram. Int.* 42 (2016) 13024–13034. doi:10.1016/j.ceramint.2016.05.081.
- [34] M. Mahajan, N.P. Lalla, K. Singh, O.P. Pandey, Synthesis and photoluminescence properties of in-situ synthesized core e shell (m-VC @ C) nanocomposites, *Mater. Chem. Phys.* 160 (2015) 48–58. doi:10.1016/j.matchemphys.2015.04.004.
- [35] A. Kumar, K. Singh, O.P. Pandey, Optimization of processing parameters for the synthesis of tungsten carbide (WC) nanoparticles through solvo thermal route, 42 (2010) 2477–2483. doi:10.1016/j.physe.2010.06.002.
- [36] L.K. Brar, G. Singla, O.P. Pandey, The role of carbon in structural evolution during single step synthesis of nano tantalum carbide, *RSC Adv.* 6 (2016) 109174–109184. doi:10.1039/C6RA24484J.
- [37] B.Y. El, W.I.N. Parth, The Structure of Dimolybdenum Carbide by Neutron Diffraction Technique*, *Acta Cryst.* 2 (1963) 202–205. doi:10.1107/S0365110X63000487.
- [38] G. Singla, K. Singh, O.P. Pandey, Williamson–Hall study on synthesized nanocrystalline

- tungsten carbide (WC), 113 (2013) 237–242. doi:10.1007/s00339-012-7531-0.
- [39] A.K. Zak, W.H.A. Majid, M.E. Abrishami, R. Youse, X-ray analysis of ZnO nanoparticles by Williamson e Hall and size e strain plot methods, *Solid State Sci.* 13 (2011) 251–256. doi:10.1016/j.solidstatesciences.2010.11.024.
- [40] S. Vives, E. Gaffet, C. Meunier, X-ray diffraction line profile analysis of iron ball milled powders, *Mater. Sci. Eng. A.* 366 (2004) 229–238. doi:10.1016/S0921-5093(03)00572-0.
- [41] K. Huang, K. Bi, C. Liang, S. Lin, W.J. Wang, T.Z. Yang, J. Liu, R. Zhang, Graphite Carbon-Supported Mo₂C Nanocomposites by a Single-Step Solid State Reaction for Electrochemical Oxygen Reduction, (2015) 1–11. doi:10.1371/journal.pone.0138330.
- [42] L. Ji, J. Wang, L. Guo, Z. Chen, In situ O₂-emission assisted synthesis of molybdenum carbide nanomaterial as an efficient electrocatalyst for hydrogen production in both acidic and alkaline media, *J. Mater. Chem. A.* 5 (2017) 5178–5186. doi:10.1039/C6TA10145C.
- [43] S. Iijima, T. Ichihashi, Y. Ando, Pentagons, heptagons and negative curvature in graphite microtubule growth, *Nature.* 356 (1992) 776–778. doi:10.1038/356776a0.
- [44] Q. Gao, X. Zhao, Y. Xiao, D. Zhao, M. Cao, A mild route to mesoporous Mo₂C-C hybrid nanospheres for high performance lithium-ion batteries., *Nanoscale.* 6 (2014) 6151–7. doi:10.1039/c3nr06678a.
- [45] Y. Luo, Z. Wang, Y. Fu, C. Jin, Q. Wei, R. Yang, In situ preparation of hollow Mo₂C-C hybrid microspheres as bifunctional electrocatalysts for oxygen reduction and evolution reactions, *J. Mater. Chem. A.* 4 (2016) 12583–12590. doi:10.1039/C6TA04654A.
- [46] K. Zhang, C. Li, Y. Zhao, X. Yu, Y. Chen, Porous one-dimensional Mo₂C-amorphous carbon composites: high-efficient and durable electrocatalysts for hydrogen generation., *Phys. Chem. Chem. Phys.* 17 (2015) 16609–14. doi:10.1039/c5cp02028j.

- [47] Y. Zhu, S. Wang, Y. Zhong, R. Cai, L. Li, Z. Shao, Facile synthesis of a MoO₂-Mo₂C-C composite and its application as favorable anode material for lithium-ion batteries, *J. Power Sources*. 307 (2016) 552–560. doi:10.1016/j.jpowsour.2016.01.014.
- [48] N.S. Alhajri, H. Yoshida, D.H. Anjum, A.T. Garcia-Esparza, J. Kubota, K. Domen, K. Takanabe, Synthesis of tantalum carbide and nitride nanoparticles using a reactive mesoporous template for electrochemical hydrogen evolution, *J. Mater. Chem. A*. 1 (2013) 12606. doi:10.1039/c3ta12984e.
- [49] A. Gaber, M.A. Abdel- Rahim, A.Y. Abdel-Latief, M.N. Abdel-Salam, Influence of calcination temperature on the structure and porosity of nanocrystalline SnO₂ synthesized by a conventional precipitation method, *Int. J. Electrochem. Sci.* 9 (2014) 81–95.
- [50] H. Wu, X. Wang, Y. Bai, L. Jiang, C. Wu, B. Hu, Q. Wei, X. Liu, N. Li, The effects of preparation temperature on microstructure and electrochemical performance of calcium carbide-derived carbon, *J. Solid State Electrochem.* 17 (2013) 2453–2460. doi:10.1007/s10008-013-2126-z.
- [51] R.A. Rather, S. Singh, B. Pal, A Cu⁺/Cu⁰-TiO₂ mesoporous nanocomposite exhibits improved H₂ production from H₂O under direct solar irradiation, *J. Catal.* 346 (2017) 1–9. doi:10.1016/j.jcat.2016.11.021.
- [52] J.A. Toledo-Antonio, R. Gutiérrez-Baez, P.J. Sebastian, A. Vázquez, Thermal stability and structural deformation of rutile SnO₂ nanoparticles, *J. Solid State Chem.* 174 (2003) 241–248. doi:10.1016/S0022-4596(03)00181-6.
- [53] Y.J. Lee, S.H. Kim, T.H. Lee, H.H. Nersisyan, K.H. Lee, M.H. Han, S.U. Jeong, K.S. Kang, K.K. Bae, J.H. Lee, Combustion synthesis and characterization of TaC, TaC/TaSi₂, and TaC/TaB nanoparticles, *Chem. Eng. Sci.* 107 (2014) 227–234.

doi:10.1016/j.ces.2013.12.015.

- [54] W. Wang, P. Liu, M. Zhang, J. Hu, F. Xing, The Pore Structure of Phosphoaluminate Cement, *Open J. Compos. Mater.* 2 (2012) 104–112. doi:10.4236/ojcm.2012.23012.
- [55] M. Thommes, Physical adsorption characterization of nanoporous materials, *Chemie-Ingenieur-Technik.* 82 (2010) 1059–1073. doi:10.1002/cite.201000064.
- [56] D. Voiry, H. Yamaguchi, J. Li, R. Silva, D.C.B. Alves, T. Fujita, M. Chen, T. Asefa, V.B. Shenoy, G. Eda, M. Chhowalla, Enhanced catalytic activity in strained chemically exfoliated WS₂ nanosheets for hydrogen evolution, *Nat. Mater.* 12 (2013) 850–855. doi:10.1038/nmat3700.
- [57] C.H. Kuo, L.K. Lamontagne, C.N. Brodsky, L.Y. Chou, J. Zhuang, B.T. Sneed, M.K. Sheehan, C.K. Tsung, The effect of lattice strain on the catalytic properties of Pd nanocrystals, *ChemSusChem.* 6 (2013) 1993–2000. doi:10.1002/cssc.201300447.
- [58] N.S. Alhajri, H. Anjum, K. Takanabe, Molybdenum carbide – carbon nanocomposites synthesized from a reactive template for electrochemical hydrogen evolution, *J. Mater. Chem. A.* 2 (2014) 10548–10556. doi:10.1039/c4ta00577e.
- [59] C. He, J. Tao, M.S. Dresselhaus, I.L. Thomas, A.R.J. Kucernak, V.N.N. Sundaram, C.G. Morales-Guio, L.-A. Stern, X. Hu, R. Subbaraman, D. Tripkovic, D. Strmcnik, K.C. Chang, M. Uchimura, A.P. Paulikas, V. Stamenkovic, N.M. Markovic, D. Voiry, H. Yamaguchi, J. Li, R. Silva, D.C.B. Alves, T. Fujita, M. Chen, T. Asefa, V.B. Shenoy, G. Eda, M. Chhowalla, D. Kong, H. Wang, Z. Lu, Y. Cui, E.J. Popczun, J.R. McKone, C.G. Read, A.J. Biacchi, A.M. Wiltrout, N.S. Lewis, R.E. Schaak, J. Tian, Q. Liu, N. Cheng, A.M. Asiri, X. Sun, R. Liu, S. Gu, H. Du, A.M. Asiri, C. Li, B. Cao, G.M. Veith, J.C. Neuefeind, R.R. Adzic, P.G. Khalifah, W.-F. Chen, K. Sasaki, C. Ma, A.I. Frenkel, N.

- Marinkovic, J.T. Muckerman, Y. Zhu, R.R. Adzic, Y. Zheng, Y. Jiao, Y. Zhu, L.H. Li, Y. Han, Y. Chen, A. Du, M. Jaroniec, S.Z. Qiao, W.-F. Chen, S. Iyer, S. Iyer, K. Sasaki, C.-H. Wang, Y. Zhu, J.T. Muckerman, E. Fujita, W.-F. Chen, J.T. Muckerman, E. Fujita, W.F. Chen, C.H. Wang, K. Sasaki, N. Marinkovic, W. Xu, J.T. Muckerman, Y. Zhu, R.R. Adzic, L.F. Pan, Y.H. Li, S. Yang, P.F. Liu, M.Q. Yu, H.G. Yang, P. Xiao, Y. Yan, X. Ge, Z. Liu, J.-Y. Wang, X. Wang, F. Banhart, J. Kotakoski, A. V. Krasheninnikov, L. Cançado, A. Reina, J. Kong, M. Dresselhaus, D.H. Youn, S. Han, J.Y. Kim, J.Y. Kim, H. Park, S.H. Choi, J.S. Lee, Y. Li, H. Wang, L. Xie, Y. Liang, G. Hong, H. Dai, C. Wan, Y.N. Regmi, B.M. Leonard, T.F. Jaramillo, K.P. Jorgensen, J. Bonde, J.H. Nielsen, S. Horch, I. Chorkendorff, E.J. Popczun, J.R. McKone, C.G. Read, A.J. Biacchi, A.M. Wiltout, N.S. Lewis, R.E. Schaak, Synthesis of nanostructured clean surface molybdenum carbides on graphene sheets as efficient and stable hydrogen evolution reaction catalysts, *Chem. Commun.* 51 (2015) 8323–8325. doi:10.1039/C5CC01240F.
- [60] B. Avasarala, P. Haldar, Electrochemical oxidation behavior of titanium nitride based electrocatalysts under PEM fuel cell conditions, *Electrochim. Acta.* 55 (2010) 9024–9034. doi:10.1016/j.electacta.2010.08.035.
- [61] B.E. Conway, B. V. Tilak, Interfacial processes involving electrocatalytic evolution and oxidation of H₂, and the role of chemisorbed H, *Electrochim. Acta.* 47 (2002) 3571–3594. doi:10.1016/S0013-4686(02)00329-8.
- [62] B. Sljukic, M. Vujkovic, L. Amaral, D.M.F. Santos, R.P. Rocha, C.A.C. Sequeira, J.L. Figueiredo, Carbon-supported Mo₂C electrocatalysts for hydrogen evolution reaction, *J. Mater. Chem. A.* 3 (2015) 15505–15512. doi:10.1039/C5TA02346G.
- [63] R. Subbaraman, D. Tripkovic, D. Strmcnik, K.-C. Chang, M. Uchimura, a. P. Paulikas, V.

- Stamenkovic, N.M. Markovic, Enhancing Hydrogen Evolution Activity in Water Splitting by Tailoring Li^+ - $\text{Ni}(\text{OH})_2$ -Pt Interfaces, *Science* (80-.). 334 (2011) 1256–1260.
doi:10.1126/science.1211934.
- [64] Z. Shi, Y. Wang, H. Lin, H. Zhang, M. Shen, S. Xie, Y. Zhang, Q. Gao, Y. Tang, Porous nanoMoC@graphite shell derived from a MOFs-directed strategy: an efficient electrocatalyst for the hydrogen evolution reaction, *J. Mater. Chem. A*. 4 (2016) 6006–6013. doi:10.1039/C6TA01900E.
- [65] K. Ojha, M. Sharma, H. Koley, A.K. Ganguli, Reduced graphene oxide and MoP composite as highly efficient and durable electrocatalyst for hydrogen evolution in both acidic and alkaline media, *Catal. Sci. Technol.* 7 (2017) 668–676.
doi:10.1039/C6CY02406H.
- [66] J.B. Jorcin, M.E. Orazem, N. Pébère, B. Tribollet, CPE analysis by local electrochemical impedance spectroscopy, *Electrochim. Acta*. 51 (2006) 1473–1479.
doi:10.1016/j.electacta.2005.02.128.

Table1. Reaction parameters, phases obtained and crystallite size

S. No	Sample Id	Temperature (°C)	Holding time (hours)	Phases obtained		Crystallite size (S)
				Major	Minor	
1	R-600/15	600	15	MoC	-	8.0
2	R-600/17	600	17	MoC	-	12.7
3	R-600/20	600	20	Mo ₂ C	C	63.6
4	R-700/12	700	12	Mo ₂ C	Mo	68.5
5	R-700/14	700	14	Mo ₂ C	C	74.9

Table 2. William-son hall analysis parameters:

Sample Id	UDM		USDM			USEDM			
	S (nm)	$\epsilon \times 10^{-3}$	S (nm)	$\epsilon \times 10^{-3}$	σ (GPa)	S (nm)	$\epsilon \times 10^{-3}$	σ (GPa)	$U \times 10^2$ (KJm ⁻³)
R-700/14	47.3	1.25	45.6	1.18	0.46	46.68	0.87	0.34	2.92
R-600/20	37.13	1.18	35.5	1.08	0.42	36.5	0.82	0.32	2.53

Figure captions

Figure 1. (a) XRD pattern of sample synthesized at 600 and 700 °C and (b) Rietveld refinement pattern of R-600/20 and R-700/20. The measured and calculated data are observed by dots and solid curve respectively.

Figure 2. Raman spectra of R-600/20 and R-700/14 samples.

Figure 3. Field emission scanning electron microscope (FESEM) images of R-700/14 (a) 500 nm, (b) 200 nm showing carbon network between the particles, (c) and (d) of R-600/20 at 500 and 200 nm, indicating the agglomeration and uniform size of the particles.

Figure 4. (a) TEM micrograph of R-700/14 (b) HRTEM of R-700/14, (c) EDS mapping TEM micrograph of R-700/14 (d) EDS elemental distribution of molybdenum (Mo), (e) distribution of carbon (C) and (f) distribution of oxygen (O).

Figure 5. (a) TEM micrograph of R-600/20 (b) HRTEM of R-600/20, (c) EDS mapping TEM micrograph of R-600/20 (d) EDS elemental distribution of molybdenum (Mo), (e) distribution of carbon (C) and (f) distribution of oxygen (O).

Figure 6. Log-normal probability distribution of particles (a) R-700/14 and (b) R-600/20.

Figure 7. XPS survey spectrum (a) R-700/14, (b) R-600/12 and HR XPS spectrum of Mo3d (c) R-700/14 and (d) R-600/20.

Figure 8. (a) Linear sweep voltammetry (LSV) before and after 2000 cycles for R-700/14 and R-600/20, (b) Tafel plot of R-700/14 and R-600/20 before and after 2000 cycles.

Figure 9. Cyclic voltammetry (CV) at different scan rates (a) R-600/20, (b) R-700/14, (c) R-600/15, (d) R-600/17, (e) R-700/12 and Electric double layer capacitance (EDLC,

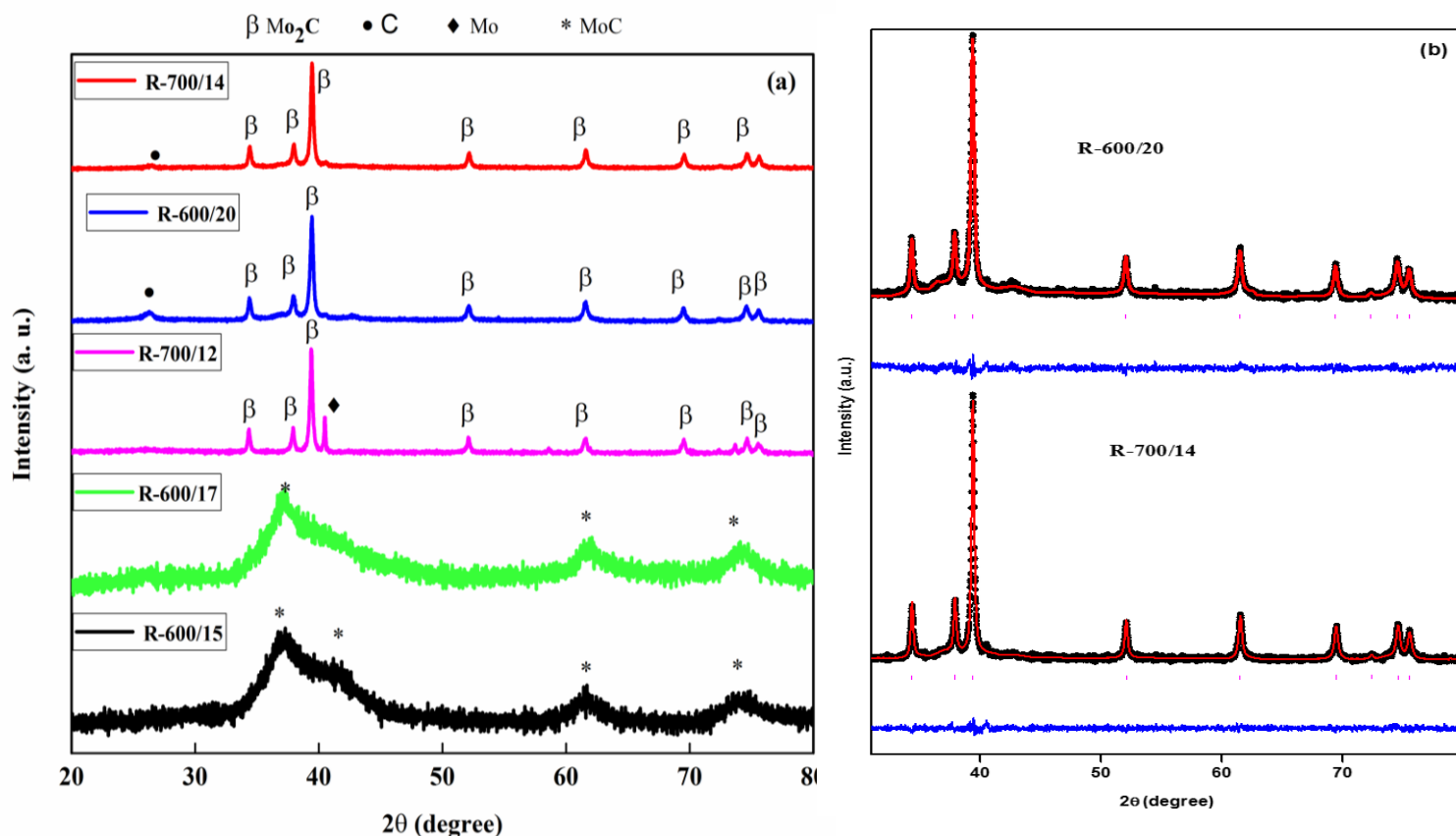


Figure 1. (a) XRD pattern of sample synthesized at 600 and 700 °C and (b) Rietveld refinement pattern of R-600/20 and R-700/20. The measured and calculated data are observed by dots and solid curve respectively.

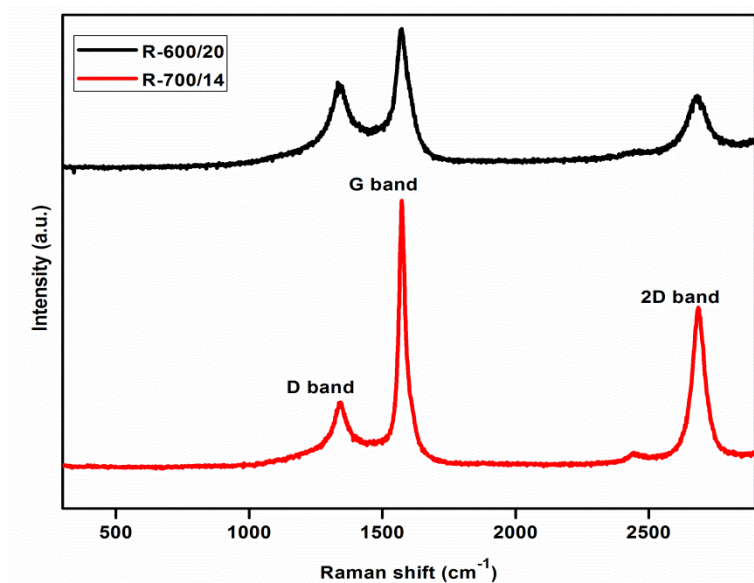


Figure 2. Raman spectra of R-600/20 and R-700/14 samples.

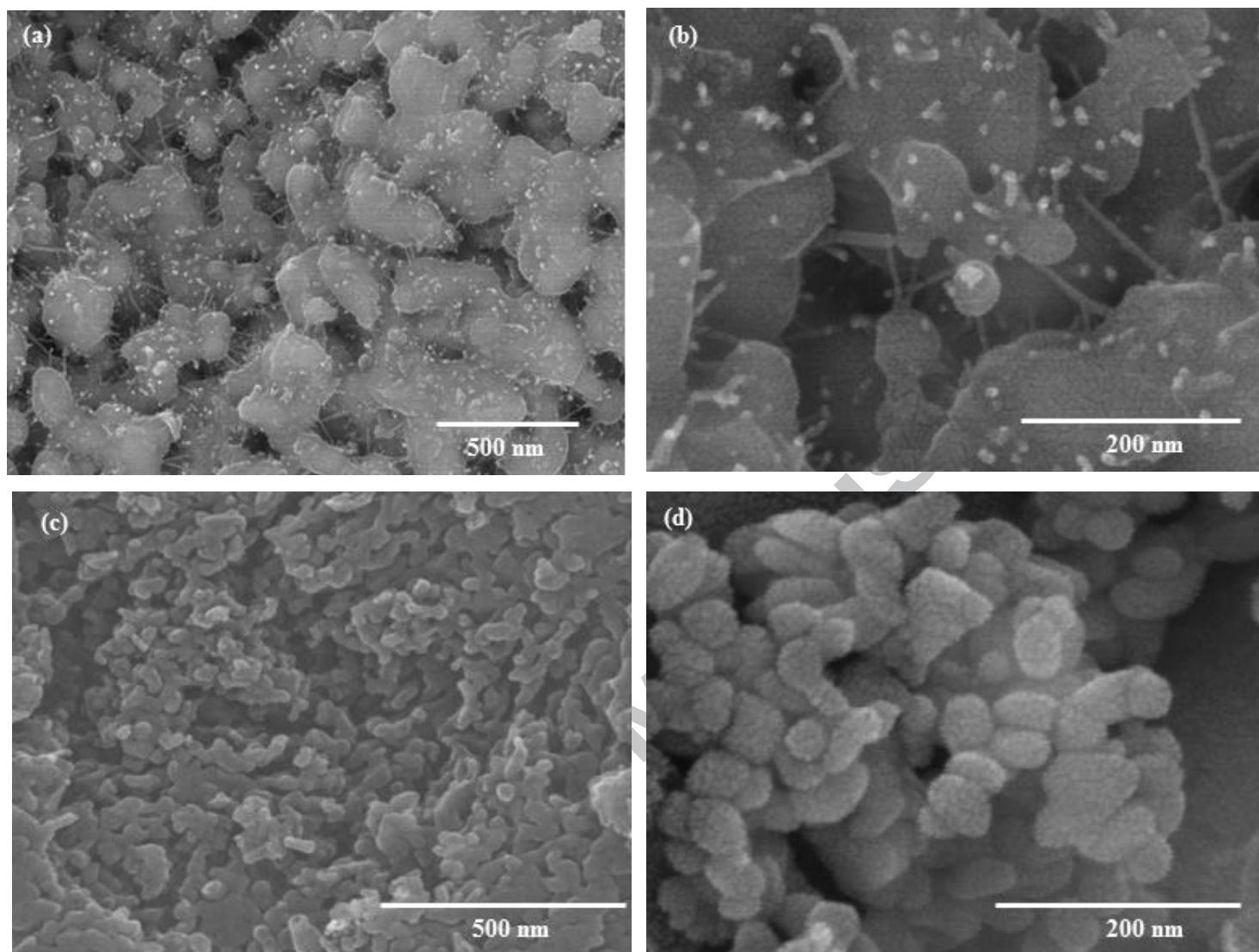


Figure 3. Field emission scanning electron microscope (FESEM) images of R-700/14 (a) 500 nm, (b) 200 nm showing carbon network between the particles, (c) and (d) of R-600/20 at 500 and 200 nm, indicating the agglomeration and uniform size of the particles.

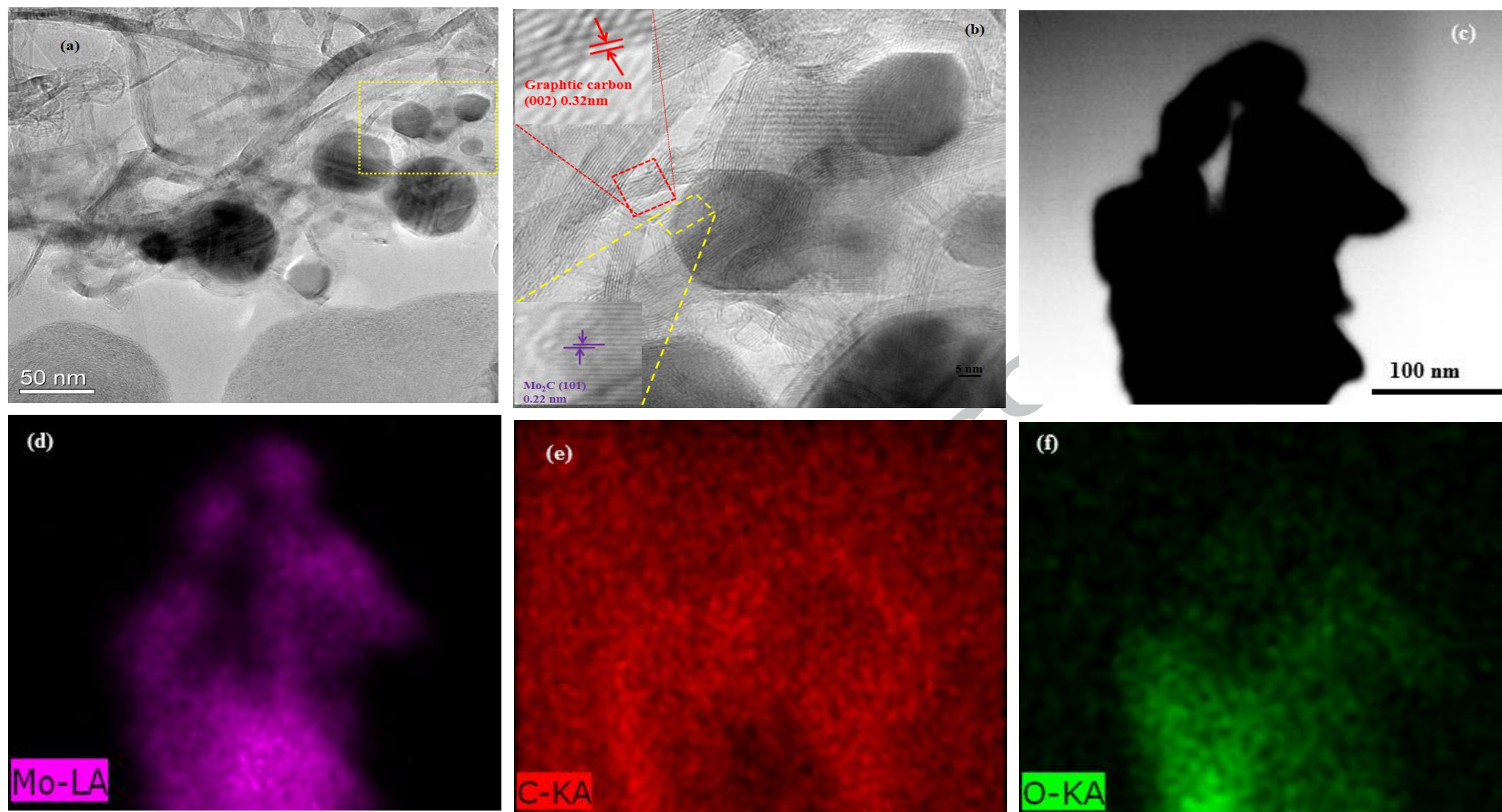


Figure 4. (a) TEM micrograph of R-700/14 (b) HRTEM of R-700/14, (c) EDS mapping TEM micrograph of R-700/14 (d) EDS elemental distribution of molybdenum (Mo), (e) distribution of carbon (C) and (f) distribution of oxygen (O).

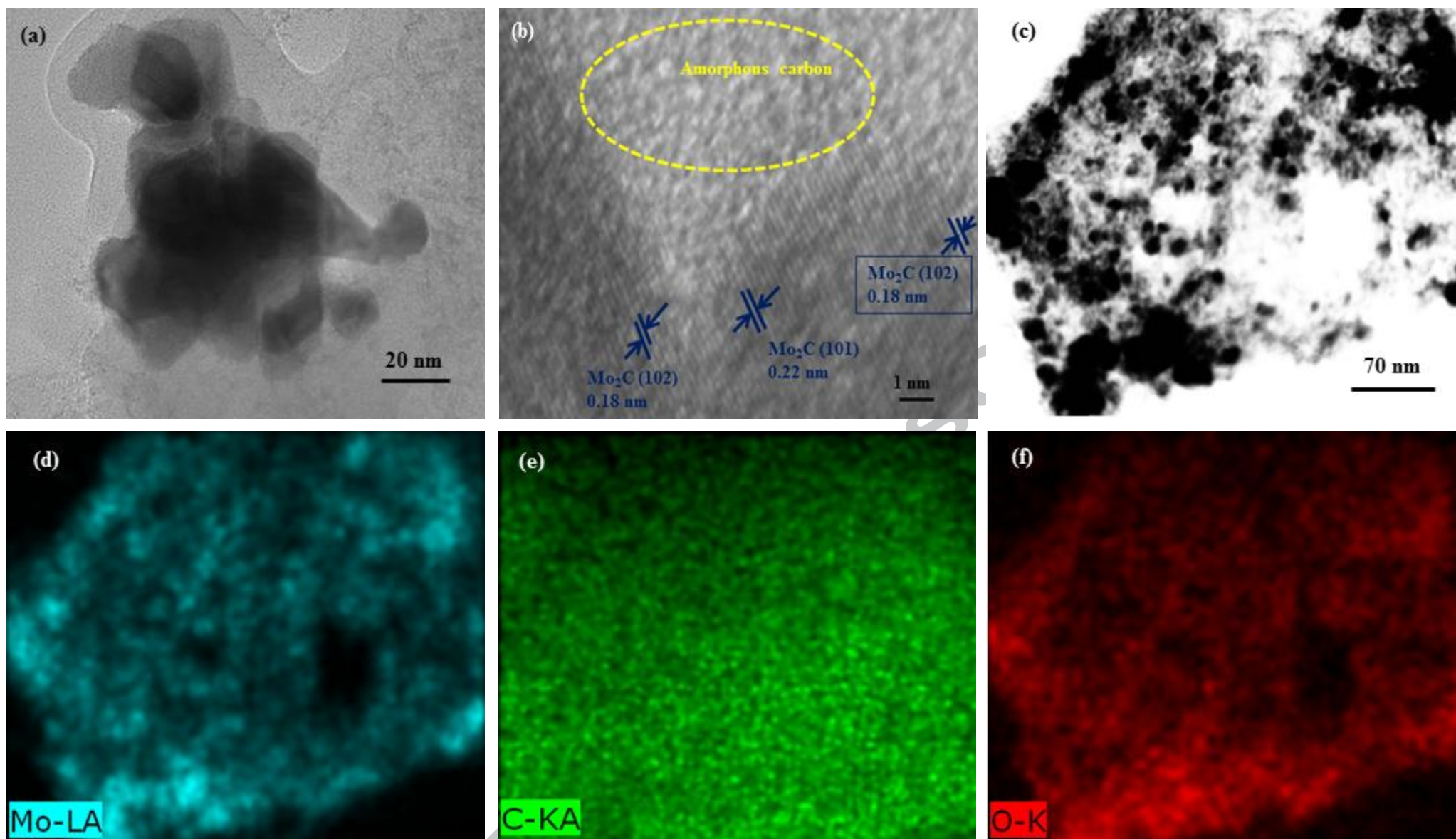


Figure 5. (a) TEM micrograph of R-600/20 (b) HRTEM of R-600/20, (c) EDS mapping TEM micrograph of R-600/20 (d) EDS elemental distribution of molybdenum (Mo), (e) distribution of carbon (C) and (f) distribution of oxygen (O).

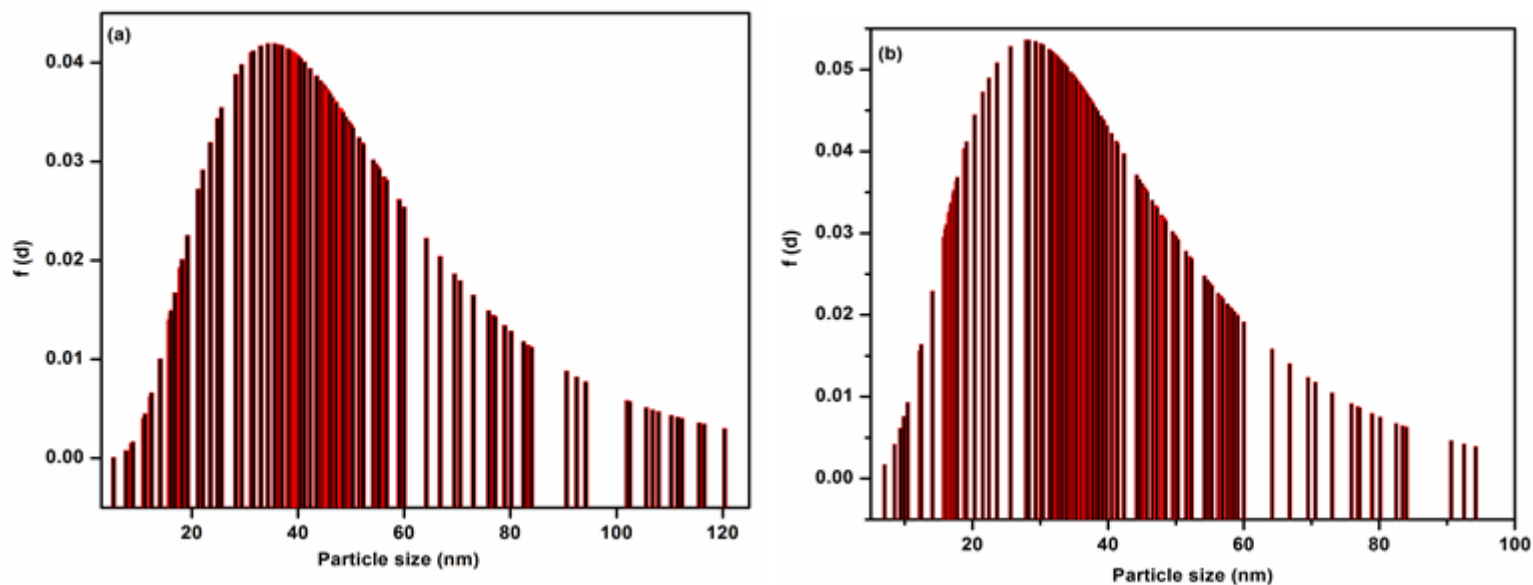


Figure 6. Log-normal probability distribution of particles (a) R-700/14 and (b) R-600/20.

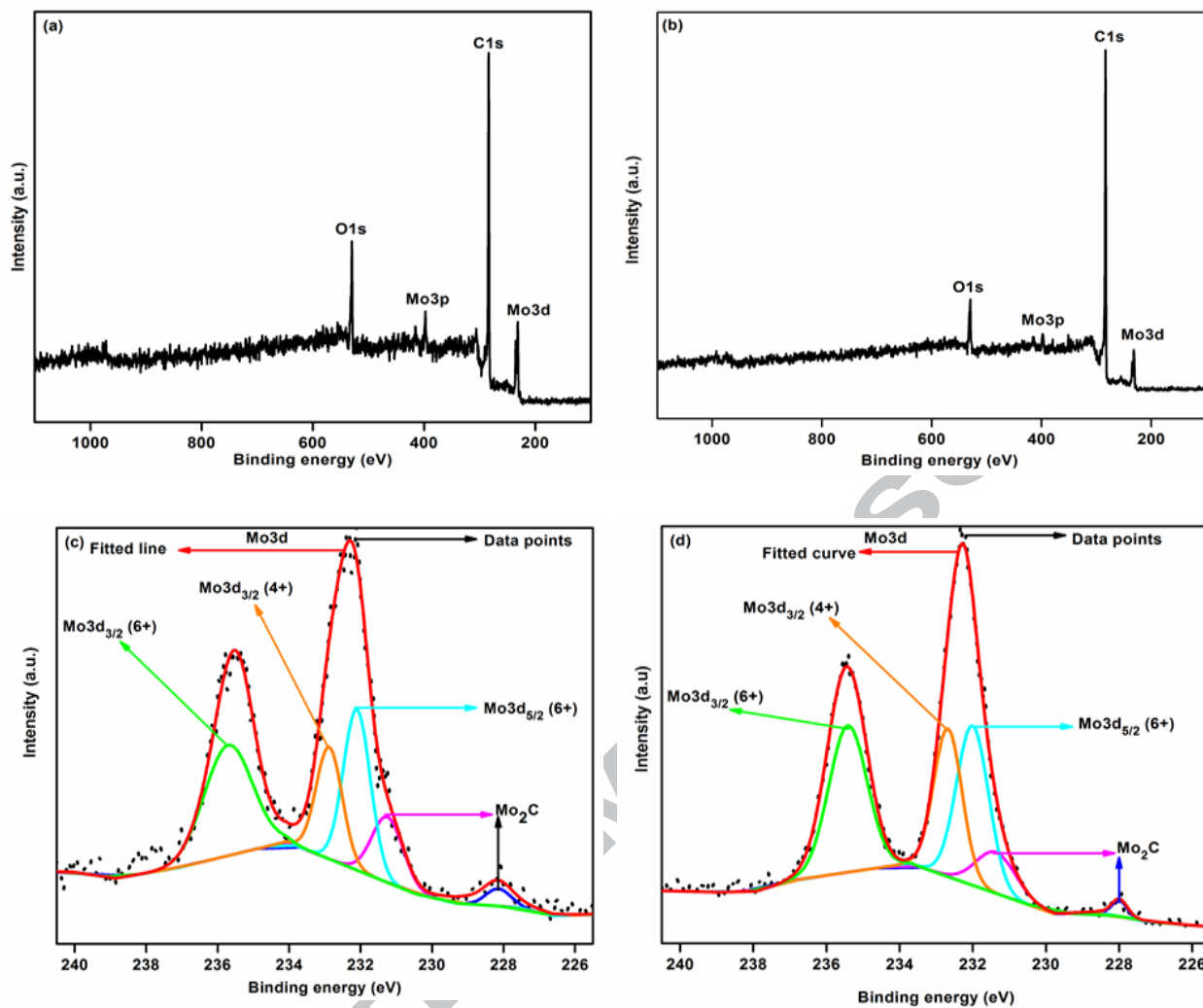


Figure 7. XPS survey spectrum (a) R-700/14, (b) R-600/12 and HR XPS spectrum of Mo3d (c) R-700/14 and (d) R-600/20.

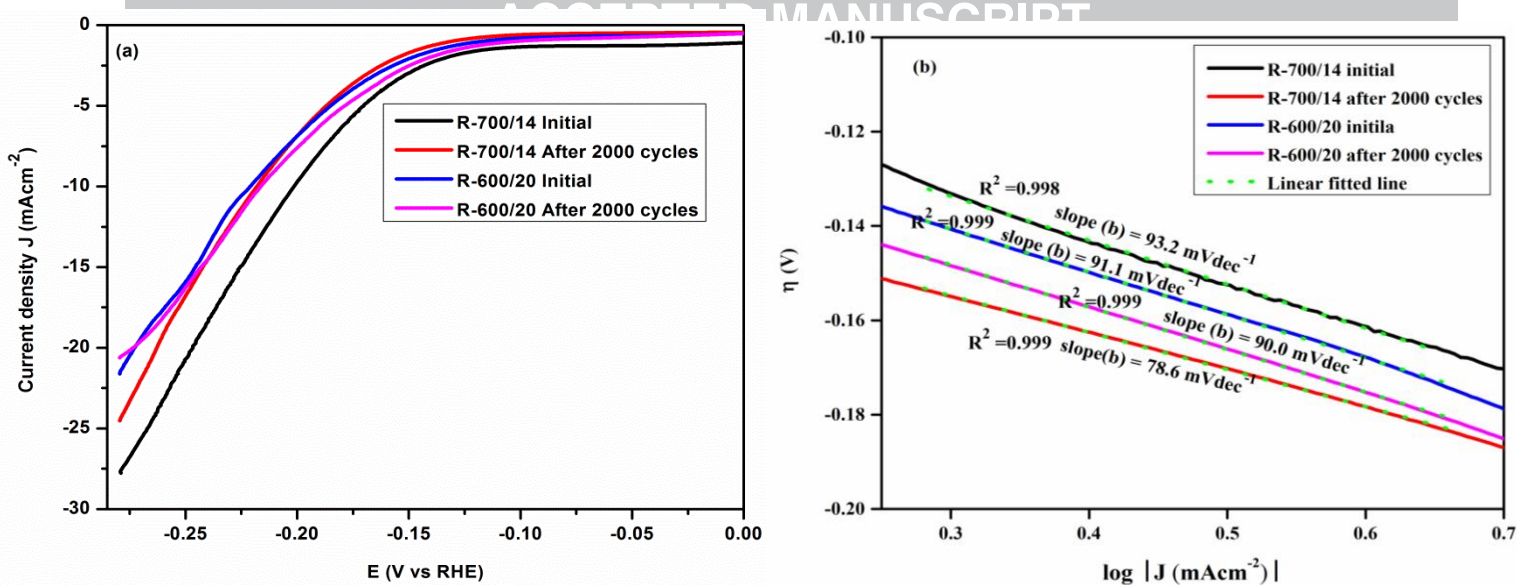


Figure 8. (a) Linear sweep voltammetry (LSV) before and after 2000 cycles for R-700/14 and R-600/20, (b) Tafel plot of R-700/14 and R-600/20 before and after 2000 cycles.

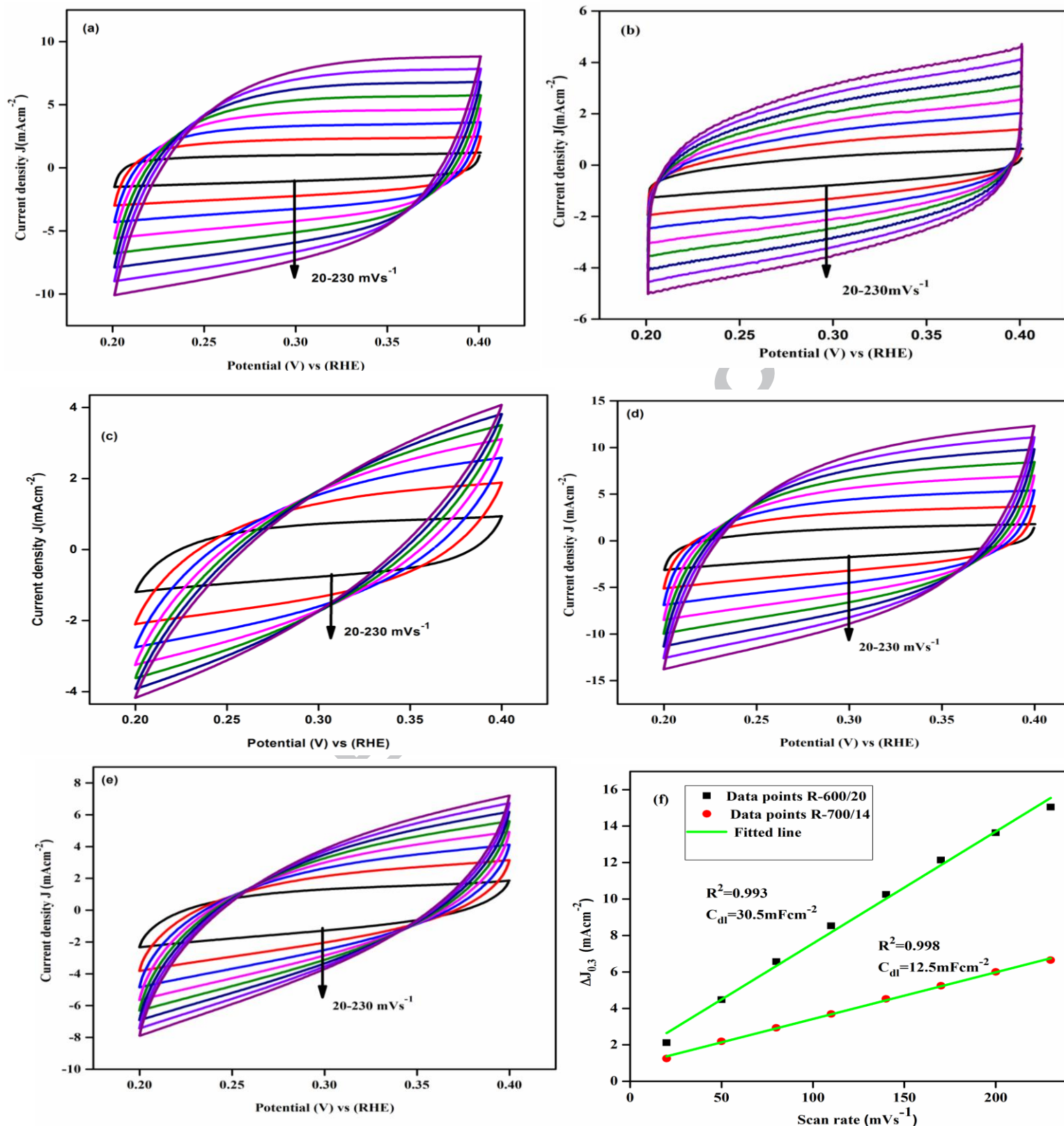


Figure 9. Cyclic voltammetry (CV) at different scan rates (a) R-600/20, (b) R-700/14, (c) R-600/15, (d) R-600/17, (e) R-700/12 and Electric double layer capacitance (EDLC, C_{dl}) of R-600/20 and R-700/14.

Highlights

- Carbon coated β -Mo₂C has been synthesized at relatively low temperature 600 °C.
- The Nature of adherent surface carbon on β -Mo₂C influences electrocatalytic activity.
- Graphitic/amorphous carbon influence the charge transfer kinetics and stability.
- EDLC results suggest β -Mo₂C suitable candidate for energy storage devices.